AAS 15-531

SPATIAL RESOLUTION IN DENSITY PREDICTION FOR DIFFERENTIAL DRAG MANEUVERING GUIDANCE

David Guglielmo[*], David Pérez[†], Riccardo Bevilacqua[‡], and Leonel Mazal[§]

Atmospheric differential drag can be used to control the relative motion of multiple coplanar spacecraft in Low Earth Orbit (LEO), without the use of any propellant, provided that they can vary their ballistic coefficients. However, the variability of the atmospheric density, and therefore the drag acceleration, makes the generation of accurate drag-based guidance a challenging problem. Currently available density models have biased results, causing errors in the drag force estimation. In this work a method for predicting the atmospheric density along the future orbit of a spacecraft is combined with a calibrator used with existing empirical atmospheric models. The combination is used to improve differential drag-based relative maneuvering by adding spatial resolution to atmospheric density prediction methods. This leads to the creation of more realistic guidance trajectories for spacecraft relative maneuvering based on differential drag.

INTRODUCTION

Formations of small satellites hold the potential for replacing large complex spacecraft, as explained in Refs. 1–4. In-orbit inspection and maintenance missions and other complex space tasks can be performed by spacecraft flying in formation. The loss of one spacecraft in a formation may not compromise the mission, providing redundancy. Additionally, smaller satellites are lighter and can be stacked in a launcher[5–7] which reduces the cost of orbit injection. Consequently, there is a growing interest in the aerospace community in the development of methods for small spacecraft autonomous formation flying.

Any formation of spacecraft requires the ability for the spacecraft involved to control their relative position and velocity, which is typically performed at high operation cost using thrusters. Hence, alternative lower-cost means to maneuver spacecraft are of great interest. Leonard et al.[8] proposed varying the cross sectional area of spacecraft to alter the drag force acting on them, as a method for controlling their relative motion at LEO. Differential drag can allow for propellant-less planar relative maneuvering, which can reduce fuel usage and costs for formation flying missions. Sensors mounted onboard spacecraft can also benefit from a cleaner environment due to the lack of thruster plumes. However, using differential drag to maneuver imposes the constraint of operating where

[*]Graduate Research Assistant, Mechanical and Aerospace Department, University of Florida, Gainesville, FL, AIAA Student Member. dguglielmo@ufl.edu

[†]Postdoctoral Research Assistant, Mechanical and Aerospace Department, University of Florida, Gainesville, FL, AIAA Member. perezd4@ufl.edu

[‡]Associate Professor, Mechanical and Aerospace Department, University of Florida, Gainesville, FL, AIAA Senior Member. bevilr@ufl.edu

[§]Postdoctoral Research Assistant, Mechanical and Aerospace Department, University of Florida, Gainesville, FL. leo.mazal@ufl.edu

the atmosphere is sufficiently dense to generate significant drag force, and limits the maneuvers to the orbital plane. Moreover, using the drag for maneuvering can increase the orbital decay of the spacecraft. Despite the downsides of differential drag, future impacts of the ideas here proposed can be foreseen for higher orbits. For example, the concept of exploiting differentials in environmental forces can be also imagined for geosynchronous satellites using solar radiation pressure.

In the last few years there have been quite a few papers inspired by Leonard's differential drag idea. Bevilacqua et al.[9,10] used the linear Schweighart and Sedwick model[11] to create a differential drag based rendezvous guidance assuming constant density. Ben-Yaacov and Gurfil[12] studied the use of differential drag for cluster-keeping purposes. Pérez and Bevilacqua[13] developed a Lyapunov-based controller for relative maneuvering of spacecraft using differential drag. Dell'Elce and Kerschen proposed the use of model predictive control[14] and a three-step optimal control approach[15] for drag based rendezvous maneuvers. There have been a few efforts for exploiting the differential drag concept in real missions. The ORBCOMM[16] constellation used differential drag for formation keeping. Also, the JC2Sat[17–20] project developed by the Canadian Space Agency (CSA) and the Japan Aerospace Exploration Agency (JAXA) proposed the use of differential drag for relative maneuvering of spacecraft within close proximity of each other extending the methodology presented by Leonard and studying implementation issues such as navigational errors.

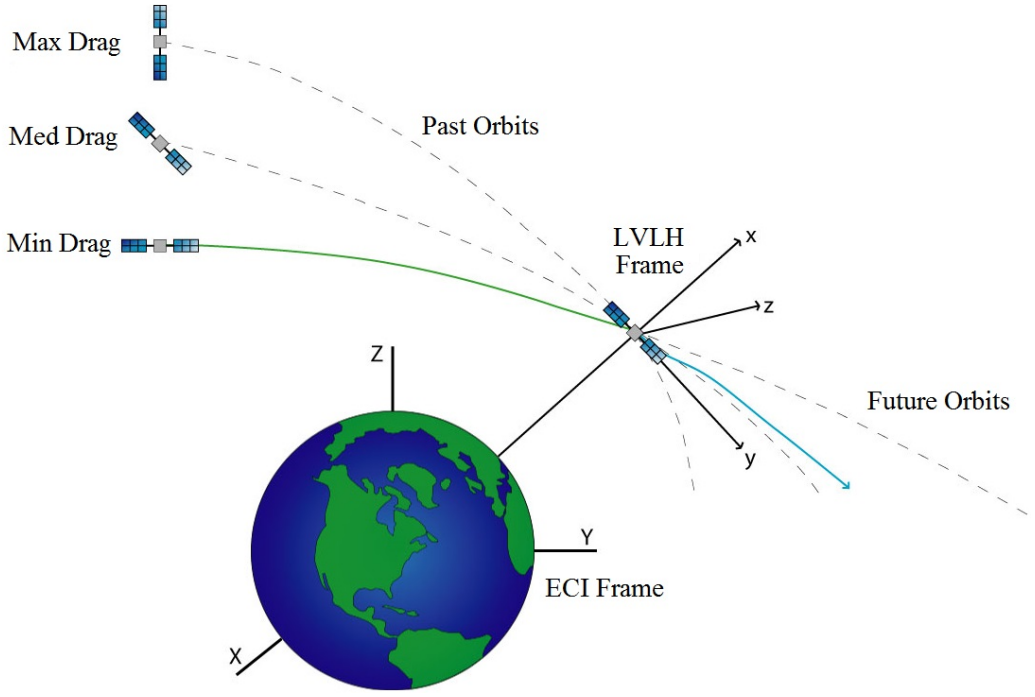

Figure 1. Concept for obtaining density in the region of space bounding all possible maneuvers, shown for a single spacecraft, showing inertial and local reference frames.

Difficulties in estimating the drag force results in lack of realism in any drag-based guidance trajectory, making tracking more difficult. In the literature on drag-based maneuvering, it is usually assumed that the density is constant for guidance and control purposes (see Refs. 10, 16, 21–23). Any guidance trajectory created under the assumption of constant density will be inaccurate due to unrealistic control forces. In Ref. 24, forecasted density was used for creating a guidance for a drag based rendezvous. The density forecasting was performed using a feed-forward neural network

predictor, similar to those developed by Pérez et al.,[25] which are limited to forecasting the density along the orbit of a non-maneuvering spacecraft (i.e., with a constant ballistic coefficient). However, perfect knowledge of the density was assumed, that is, modeling or measuring errors were not accounted for. Furthermore, the predicted density was assumed to be constant in space regardless of the position of the spacecraft at a given time. As a consequence of this the density at the target and chaser positions were the same throughout the guidance.

In this work, a linear fit density calibrator (inspired by the one developed by Pérez and Bevilacqua[26]) is introduced to provide to simulate estimation of real atmospheric density data from density calculated using existing atmospheric models. DTM-2013,[27] a high-accuracy density model, is used to represent observed density, while NRLMSISE-00[28] and JB2008[29] are used as inputs to the calibrator. The use of this calibrator accounts for modeling errors in the creation of the guidance. The calibrator is used in conjunction with recurrent neural network density predictors similar to those developed in Ref. 25 to forecast atmospheric density, allowing the design of guidance trajectories for differential drag-based maneuvering.

To create the guidance, the orbits of chaser and target are propagated in the past along three orbits. These orbits (Past Orbits in Figure 1) correspond to trajectories with the minimum (minimum drag), half (medium drag) and maximum (maximum drag) available drag area deployed. The calibrator is used to estimate the density along these three orbits. It should be noted that the actual orbit of the spacecraft corresponds to the case with the minimum area (in green in Figure 1). These orbits extend back in time from the beginning of the maneuver (epoch time) to eight days into the past, which includes all training and testing data sets, as well as the two days of data used for forecasting. Using the density along these orbits, the density predictors are used to forecast the density in the future along them (Future Orbits in Figure 1). This provides the guidance and control systems of the spacecraft with predicted density values along the future orbits covering the region in space in which the maneuver will take place, The guidance trajectory (in blue in Figure 1), is then created by propagating the controlled dynamics of the spacecraft and interpolating the density from the nearest points in the future orbits to the current position of the spacecraft in the guidance trajectory, thus providing the spatial resolution.

The guidance methodology presented in this work assumes that two spacecraft (chaser and target) have the capability to vary their ballistic coefficient (for example by deploying or retracting a set of drag surfaces), thus changing the magnitude of the aerodynamic drag. The reference frame used in this work for representing spacecraft relative motion is the Local Vertical Local Horizontal (LVLH) reference frame, which is assumed to be attached to the target spacecraft. Figure 1 shows the Earth-Centered Inertial frame (lower left) and the LVLH frame (upper right). In the LVLH frame $\hat{x}$ points from the origin of the ECI (Earth-Centered Inertial) frame to the target spacecraft, $\hat{z}$ points in the direction of angular momentum of the target's orbit, and $\hat{y}$ completes the right-handed frame.

Given that the out of plane component of the aerodynamic force is very small, atmospheric differential drag can provide effective control only in the orbital plane ($\hat{x}$ and $\hat{y}$). Hence, the discussion presented in this work will be limited to in-plane motion, assuming that out-of-plane ($\hat{z}$) motion is controlled by different means. The attitude of the spacecraft is also assumed to be stabilized. Additionally it is assumed that the control is either positive maximum (higher drag on the target), negative maximum (higher drag on the chaser), or zero (minimum drag on both spacecraft), as previously done in Refs. 9, 18–20, neglecting the time required by the surfaces to be deployed or retracted. The time required to deploy or retract the surfaces (on the order of seconds) is negligible with respect to the maneuver duration (on the order of days).

This paper presents the following advances in the state of the art:

1. Spatial resolution is used to improve the accuracy of forecasted density.
2. A calibrator, that approximates density estimated by the DTM-2013 atmospheric model taking as inputs the densities estimated by the JB2008 and NRLMSISE-00 atmospheric models, is used to account for imperfect knowledge of the density.
3. Recurrent neural network predictors are used to forecast the calibrated density from past density along a given orbit for several orbits resulting from varied drag configurations.
4. Guidance trajectories are created for a rendezvous maneuver between two spacecraft, leveraging the spatial resolution described above to interpolate the predicted density to provide a more accurate estimation of the drag force at each timestep.
5. The benefit of adding spatial resolution for the drag-based guidance is shown to vary for periods of low and high geomagnetic activity.

This paper is organized as follows. The first section presents the drag acceleration and atmospheric density, along with a calibrator designed for approximating density estimated by DTM-2013 and a predictor for forecasting density along a given orbit. The second section presents the basics for spacecraft relative maneuvering using differential drag, including the nonlinear orbital dynamics and linear relative dynamics equations, a Lyapunov controller designed for drag relative maneuvering and the methodology presented for creating the guidance. The third section presents the results for the numerical simulations. Finally the fourth section contains the conclusions.

ATMOSPHERIC DENSITY AND DIFFERENTIAL DRAG

After gravity, atmospheric drag is the largest force acting on spacecraft at altitudes below 700 km. Proper understanding of the drag acceleration will allow for precise on orbit determination and can be used for creating realistic guidance trajectories for drag-based maneuvering. The drag acceleration affecting spacecraft in LEO is a function of the atmospheric density and winds, and orbital velocity, geometry, attitude, drag coefficient and mass of the spacecraft. Many of parameters must be estimated, producing errors in the modeling of the drag force. This causes large uncertainties regarding the control forces available for drag-actuated maneuvers. The differential drag acceleration for target and chaser in similar flow conditions is expressed with the following:

$$\vec{a}_{D_{rel}} = -\frac{1}{2}\left(\rho_C B_C \vec{v}_C |\vec{v}_C| - \rho_T B_T \vec{v}_T |\vec{v}_T|\right) \tag{1}$$

where $B = \frac{C_D A}{m}$ and v represents the speed of a spacecraft through a medium. The subscript T denotes the target, and C denotes the chaser spacecraft. According to Vallado,[30] this approximation of the drag acceleration holds true for a body in viscous flow, in which the time scale of collisions between the body and gas particles is much smaller than the time scale of particle-particle collisions. Furthermore, the equation also assumes that the two spacecraft are in similar flow conditions, and have identical mass m. Doornbos et al.[31] indicate that density can vary by more than one order of magnitude at a given time and location as a result of different solar and geomagnetic conditions, which highlights the importance of proper density modeling for the creation of drag based relative maneuvering guidance.

The atmospheric density can be estimated using atmospheric models, which can be classified into physics-based and empirical models. The physics-based models can be more accurate but suffer from bias caused by poor representation of the underlying physics (see Ref. 32), and are computationally expensive due to the high number of variables used and the size of the spatial volume they model. In contrast, empirical models, which rely on observed data, are less computationally expensive. However, since data are not available for all locations and times, biases in the estimated density can result due to behavior not captured in the observed data (as shown in Ref. 33). In this work three empirical atmospheric models (DTM-2013,[27] JB2008[29] and NRLMSISE-00[28]) are used for modeling the density.

Solar and geomagnetic effects significantly influence atmospheric density; an example can be observed in the evolution of the atmospheric density during the 2003 Halloween solar storm, as explained by Bruinsma et al.[34] Additionally, Walterscheid[35] provides an explanation of the increase in atmospheric density due to geomagnetic activity; solar EUV (Extreme UltraViolet) radiation excites air molecules, with only local effects. The lower molecular weight air molecules in the affected region then move to higher altitudes and are replaced by higher molecular weight particles, increasing the average local mass density while leaving pressure unchanged.

Data Sets

Two time intervals in January 2005, were chosen for creating and testing the rendezvous guidance trajectories. January 18^{th} 2005 at 00:00:00 UTC and January 27^{th} 2005 at 00:00:00 UTC were used as the epoch times for the rendezvous maneuvers. As can be seen in Figure 2, these two maneuver times were chosen since they correspond respectively to periods of sustained high and low K_p (a proxy index for geomagnetic activity) in January 2005. These dates are chosen to clearly represent the effect of K_p on the guidance. The data sets used for the inputs and targets for the predictor and calibrator are shown below in Tables 1 and 2.

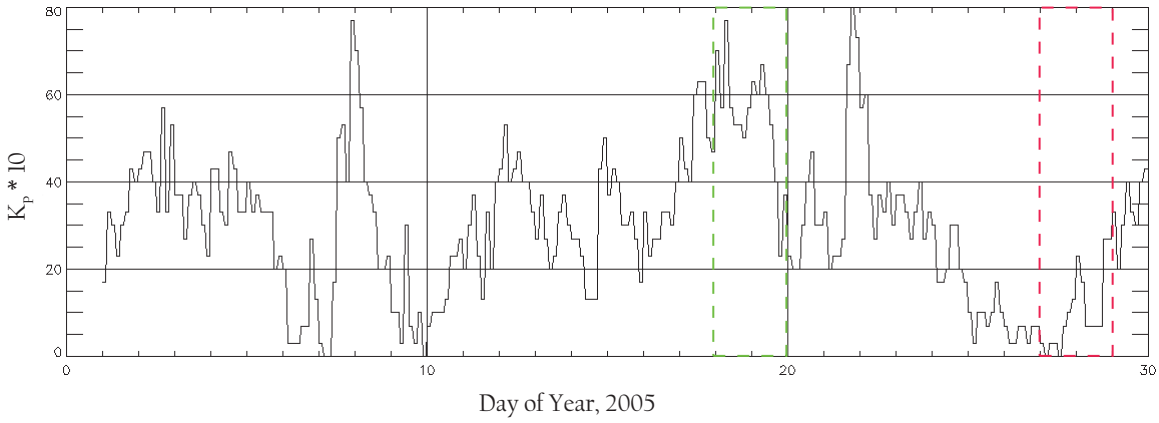

Figure 2. Geomagnetic Activity as Represented by K_p in January 2005, with Sustained High K_p Boxed in Green and Sustained Low K_p Boxed in Orange

Calibrator for Empirical Atmospheric Models

Table 1. Data Used for Calibrator

	JB2008/NRLMSISE-00	DTM-2013
Calibrator Fit Data	1/10/2005-1/13/2005	1/10/2005-1/13/2005
Calibrator Test Data	1/14/2005-1/17/2005	1/14/2005-1/17/2005

The calibrators presented in Ref. 26 were designed to assimilate measurements of atmospheric density, and combine the estimates of empirical models in order to improve density estimation. In this work a calibrator was developed that takes as input the estimated density by the empirical atmospheric models JB2008[29] and NRLMSISE-00[28] (ρ_{JB} and ρ_{MSIS}, respectively), and outputs value for the density ($\rho_{DTM}\prime$) calibrated to approximate the density as modeled by DTM-2013[27] (ρ_{DTM}), which represents the real density in this work. A linear fit model was used as the calibrator, which consists of a weighted sum of the density of JB2008, NRLMSISE-00, and a bias to correct the output, as shown in the following equation:

$$\rho_{DTM}\prime = w_1 \cdot \rho_{JB,S} + w_2 \cdot \rho_{MSIS,S} + b, \tag{2}$$

$$w_1 = 9.46 \cdot 10^{-5}, \quad w_2 = 2.808 \cdot 10^{-4}, \quad b = 1.04 \cdot 10^{-3} {}^{kg}/_{m^3} \tag{3}$$

The weights (w_1 and w_2), and the bias (b) were found in MATLAB using a least-squares method to find the weights and bias minimizing the error. The data used to find the weights and the offset (denoted fit data set) consists of input-output pairings, with JB2008 and NRLMSISE-00 densities as inputs, and simultaneous DTM-2013 densities as targets (see Table 1). All data for the calibrator fit were taken from the high K_p, min drag data set for the target. Over the fit data set the Pearson correlation coefficient (r) between DTM-2013 and the calibrated density was 0.916 and the mean squared error (MSE) was $1.168 \cdot 10^{-8} {}^{kg^2}/_{m^6}$. The calibrator was applied on a test data set, consisting of similar input-output pairings (explained in Table 1), to verify its generalization capability. Over the test data set, the r was 0.930 and the MSE was $6.411 \cdot 10^{-8} {}^{kg^2}/_{m^6}$.

The inputs to the calibrator are scaled according to Eqns. (4). Scaling the data according to the mean and standard deviation allows for improved finite-precision computational accuracy. The subscript S denotes scaled data.

$$\rho_{JB,S} = \frac{\rho_{JB} - \mu_{JB}}{\sigma_{JB}}, \quad \rho_{MSIS,S} = \frac{\rho_{MSIS} - \mu_{MSIS}}{\sigma_{MSIS}} \tag{4}$$

$$\mu_{MSIS} = 1.141 \cdot 10^{-3} \ {}^{kg}/_{m^3} \quad \mu_{JB} = 9.580 \cdot 10^{-4} \ {}^{kg}/_{m^3}$$

$$\sigma_{MSIS} = 3.429 \cdot 10^{-4} \ {}^{kg}/_{m^3} \quad \sigma_{JB} = 3.594 \cdot 10^{-4} \ {}^{kg}/_{m^3}$$

The means (μ), and standard deviations (σ) are those of JB2008 and NRLMSISE-00 densities in the fit data set.

Predictors for Future Density

Three recurrent neural networks (such as the one shown in Figure 3), denoted predictors, are used to forecast density two days into the future along an orbit from past calibrated density. The neural networks used have two layers (input and output layer), and have delays in the input and in the feedback loop. The delays provide temporal context of the inputs and the outputs to the

Table 2. Data Used for Predictors

	Dates Used
Training and Validation Delays, High K_p	1/10/2005-1/11/2005, Calibrated Density
Training and Validation Delays, Low K_p	1/19/2005-1/20/2005, Calibrated Density
Training and Validation Inputs, High K_p	1/12/2005-1/13/2005, Calibrated Density
Training and Validation Inputs, Low K_p	1/21/2005-1/22/2005, Calibrated Density
Training and Validation Targets, High K_p	1/14/2005-1/15/2005, Calibrated Density
Training and Validation Targets, Low K_p	1/23/2005-1/24/2005, Calibrated Density
Testing Delays, High K_p	1/12/2005-1/13/2005, Calibrated Density
Testing Delays, Low K_p	1/21/2005-1/22/2005, Calibrated Density
Testing Inputs, High K_p	1/14/2005-1/15/2005, Calibrated Density
Testing Inputs, Low K_p	1/23/2005-1/24/2005, Calibrated Density
Testing Targets, High K_p	1/16/2005-1/17/2005, Calibrated Density
Testing Targets, Low K_p	1/25/2005-1/26/2005, Calibrated Density
Forecasting Goal, High K_p	1/18/2005-1/19/2005, DTM-2013
Forecasting Goal, Low K_p	1/27/2005-1/28/2005, DTM-2013

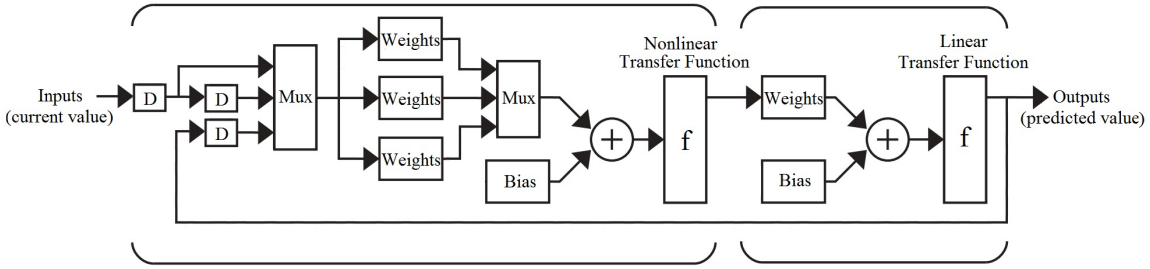

Figure 3. A sample recurrent neural network with three neurons in the input layer and two delays in the input (adapted from Ref. 25)

networks, thus improving their forecasting ability. Training of the predictors (adjusting the weights) was accomplished with the use of the Levenberg-Marquardt algorithm and using the MSE as the performance function. MathWorks recommends the use of the Levenberg-Marquardt method as a first choice for training the neural networks, due to its speed compared to other methods. Network validation is used to prevent overfitting, that is, the network memorizing the training data set. The validation consists in evaluating the network during training on a different data set (validation set), if the network's MSE for the validation set increases a predetermined number of times in subsequent validations during training (the default of 6 times is used), the training process is stopped to prevent overfitting.

A propagator (modeling the dynamics described by Eqn. (5)) written in MATLAB was used to propagate from the initial conditions (IC) of the target and chaser spacecraft at the epoch time. Using the calibrated density, the position and velocity of each spacecraft were propagated backwards for eight days for each of the orbits (min, med and max drag). This was done to accumulate sufficient data for training and testing the predictor neural networks. The two sets of dates (representing high and low geomagnetic activity) used for the maneuvers are shown in Table 2.

Training and validation of the networks is accomplished using the calibrator outputs from days six to four prior to the epoch time as inputs, with the density data from days four to two prior to the epoch to the epoch time as the targets. The validation data set consists of a random sampling of 30% of the aforementioned data set, thus leaving 70% for training. A test was performed for each network over the combined training and validation data sets. Forecasting was performed using the density data from the two days prior to the epoch as the inputs, using the predictors open-loop.

To find the appropriate number of delays in the input layer and in the feedback loop, and the number of neurons in the input layer (the number of neurons in the output layer was fixed at one), each parameter was varied, while keeping the others fixed. The ranges tried were 1-5 (increment of 1) neurons in the hidden layer, 10-200 (increment of 10) delays in the input layer, and 1-10 (increment of 1) delays in the feedback loop. Ten iterations for each parameter combination were run in an effort to avoid stopping at training error local minima during the training process. The neural network with the parameter combination with the lowest MSE over the combined training and validation data sets was chosen to be used for creating the guidance. Table 3 shows the parameters that produced the predictors with the lowest MSE for each case.

Table 3. Predictor Neural Network Details

Predictor	Input Delays	Feedback Delays	Hidden Layer Neurons
Min Drag, High K_p	10	4	3
Min Drag, Low K_p	20	1	1
Med Drag, High K_p	100	5	3
Med Drag, Low K_p	20	2	1
Max Drag, High K_p	10	3	3
Max Drag, Low K_p	200	4	4

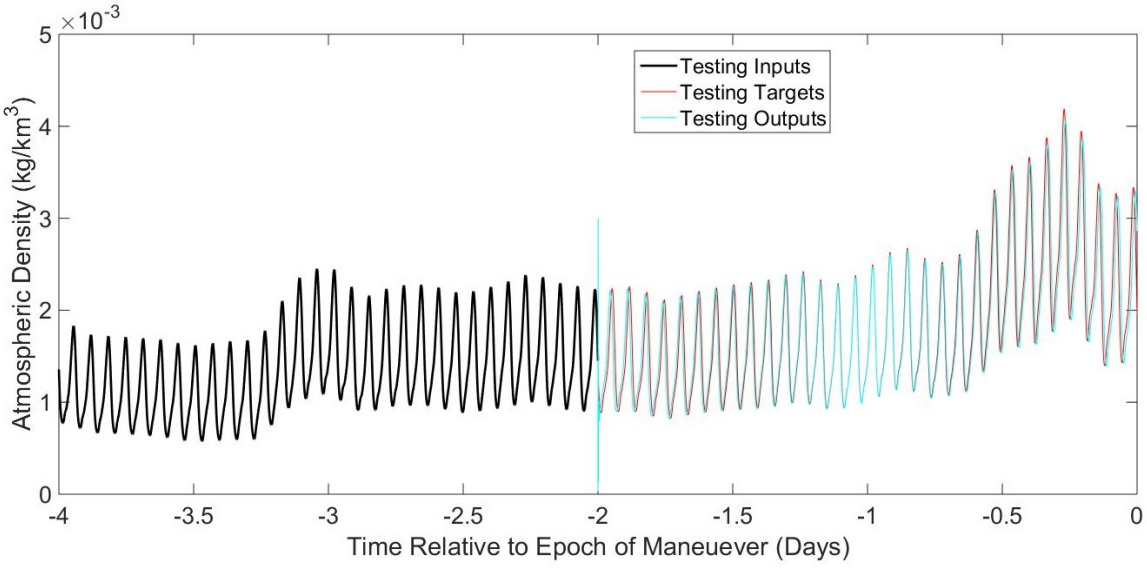

Figure 4. Forecasted and Calibrated Density for Minimum Drag Configuration on Testing Data Set, High K_p

The semi-major axis of each of the three trajectories (min, med and max drag orbits in Figure 1) evolve differently due to the difference in the drag acceleration. This results in slightly different orbital periods, as the time moves further from the epoch. Consequently, the time evolution of the density diverges as time moves away from the epoch time. Therefore, three different recurrent neural network predictors are used, one for each of the three past trajectories. All the predictors were trained using data from the target, and are used for forecasting the orbits of both the target and chaser. A sample forecast is shown in Figure 4. The neural network shown was trained on the density data for the min drag case of the high K_p maneuver. Figure 4 shows the inputs and outputs of the neural network. The remaining neural networks exhibit similar behavior. Table 4 summarizes the performance of each predictor.

Table 4. Predictor Metrics for Training and Testing

ANN Predictor	r	MSE kg^2/m^6
Min Drag, Training, High K_p	0.999	$1.129{\cdot}10^{-10}$
Min Drag, Training, Low K_p	0.989	$4.190{\cdot}10^{-9}$
Min Drag, Testing, High K_p	0.997	$2.385{\cdot}10^{-9}$
Min Drag, Testing, Low K_p	0.985	$9.555{\cdot}10^{-9}$
Med Drag, Training, High K_p	0.999	$1.248{\cdot}10^{-11}$
Med Drag, Training, Low K_p	0.951	$8.888{\cdot}10^{-9}$
Med Drag, Testing, High K_p	0.987	$2.053{\cdot}10^{-8}$
Med Drag, Testing, Low K_p	0.950	$2.259{\cdot}10^{-8}$
Max Drag, Training, High K_p	0.999	$3.364{\cdot}10^{-11}$
Max Drag, Training, Low K_p	0.935	$9.677{\cdot}10^{-9}$
Max Drag, Testing, High K_p	0.998	$2.455{\cdot}10^{-9}$
Max Drag, Testing, Low K_p	0.855	$1.244{\cdot}10^{-7}$

RELATIVE MANEUVERING WITH DIFFERENTIAL DRAG

Nonlinear Orbital Dynamics

The nonlinear orbital dynamics of the spacecraft, including two body forces, the J_2 perturbation, and drag acceleration, are represented using the following expressions:

$$\ddot{\vec{r}} = \begin{bmatrix} \ddot{X}_n \\ \ddot{Y}_n \\ \ddot{Z}_n \end{bmatrix} = \left(\frac{-\mu}{r_n^3}\right) \begin{bmatrix} X_n \\ Y_n \\ Z_n \end{bmatrix} \left(1 - \frac{3}{2} \cdot J_2 \cdot \frac{{R_e}^2}{r}\right) \begin{bmatrix} 5 \cdot \frac{Z_n^2}{r^2} - 1 \\ 5 \cdot \frac{Z_n^2}{r^2} - 1 \\ 5 \cdot \frac{Z_n^2}{r^2} - 3 \end{bmatrix} - \frac{1}{2} \cdot \rho \cdot \begin{bmatrix} \dot{X}_n \\ \dot{Y}_n \\ \dot{Z}_n \end{bmatrix} \cdot \left| \begin{bmatrix} \dot{X}_n \\ \dot{Y}_n \\ \dot{Z}_n \end{bmatrix} \right| \cdot B \quad (5)$$

These nonlinear dynamics (taken from Alfriend et al.[36]) are used to propagate both the target and chaser when tracking the guidance, but are used to propagate only the target spacecraft when creating the guidance.

Linear Relative Dynamics

Assuming that the orbit of the target is circular and that the separation between spacecraft is small, the dynamics of the chaser relative to the target can be propagated using a linear model

when creating the guidance. This is done in this work to reduce the computational cost of creating the guidance. In this work the Schweighart and Sedwick model is used for this purpose since it includes the averaged J_2 perturbation. For motion restricted to the orbital plane, the Schweighart and Sedwick model is given by:

$$\dot{\vec{x}} = \underline{A} \cdot \vec{x} + \vec{B} \cdot a_{D_{rel}}, \quad \underline{A} = \begin{bmatrix} 0 & 0 & 1 & 0 \\ 0 & 0 & 0 & 1 \\ b & 0 & 0 & a \\ 0 & 0 & -a & 0 \end{bmatrix}, \quad \vec{B} = \begin{bmatrix} 0 \\ 0 \\ 0 \\ 1 \end{bmatrix} \tag{6}$$

where a and b are defined by:

$$a = 2 \cdot n \cdot c, \quad b = (5 \cdot c^2 - 2)n^2, \quad c = \sqrt{1 + \frac{3 \cdot J_2 \cdot R_e^2}{8 \cdot}^2_{tar}}(1 + 3 \cdot cos(2 \cdot i_{tar})) \tag{7}$$

with n, $\bar{a}_{ref}$ and i_{tar} being the mean motion, mean semi-major axis and mean inclination of the target's orbit, respectively. R_e represents the Earth's mean equatorial radius.

Lyapunov Controller

In Ref. 37 a control law was presented for the actuators of the surfaces which generate the differential drag using a Lyapunov approach. The control law is used to force the nonlinear model (i.e. the dynamics of the target and chaser spacecraft) to track the guidance trajectory. The value of the control signal is selected based on the following quadratic function of the tracking error and its time derivative:

$$\begin{aligned} V &= \vec{e^T} \cdot \underline{P} \cdot \vec{e} \\ \vec{e} &= \vec{x}_n - \vec{x}_t \\ \dot{V} &= 2 \cdot \vec{e^T} \cdot \underline{P} \left(\vec{f}(\vec{x}_n) - \dot{\vec{x}}_t + \vec{B} \cdot a_{D_{rel}} \cdot \hat{u} \right) \end{aligned} \tag{8}$$

where $\hat{u}$ is the command sent to the surface actuators, matrix $\underline{Q}$ is chosen such that a Lyapunov equation is satisfied ($\underline{A}_d^T \underline{P} + \underline{P} \underline{A}_d = -\underline{Q}$), and matrices $\underline{A}_d$ and $\underline{B}$ represent a stabilized Schweighart and Sedwick model. The resulting control law presented in Ref. 37 can be expressed as:

$$\hat{u} = -sign(\vec{e^T} \cdot \underline{P} \cdot \vec{B}) \tag{9}$$

A negative control signal $\hat{u}$ is interpreted as a signal to increase the area of the chaser relative to the target, and a positive control signal is interpreted as the opposite. A zero control signal can only result from a zero tracking error in relative position and velocity, and so is interpreted as a signal to reduce the area of both spacecraft to preserve the orbit. The simulations presented use a variable timestep for the integration, but the control law in Eqn. (9) is applied every 10 minutes when creating the guidance, which allows sufficient time for the controller to alter the orbit significantly between updates. The density is updated at intervals of 60 seconds, which is the sampling rate used for the predictors. When tracking the guidance, the control law is applied once every minute.

The calibrator and predictor described in the previous sections are used to generate the density along the three orbits in the future (min, med and max drag). The guidance is then generated, utilizing the control law in Eqn. (9) using the forecasted density to propagate each spacecraft. As mentioned before, the dynamics of the target are propagated using the nonlinear dynamics in Eqn. (5), while the linear relative dynamics in Eqn. (6) are used for propagating the chaser in relation to the target. At each timestep, the density for each spacecraft is interpolated from the forecasted density for that spacecraft, based on its location. The Lyapunov-based controller is used to determine the control input (surface deployed or retracted for each spacecraft), based on the position and velocity of the chaser relative to the target. The interpolated density values are used to calculate the drag acceleration at each time step of the guidance, thus making it more realistic. The resulting guidance utilizes the interpolation to account for the spatial distribution of the guidance; therefore, it is denoted the spatial resolution guidance.

The process of creating a relative guidance trajectory is illustrated in Figure 5. Once the density has been forecasted (steps 1-3) and the projected trajectories for each spacecraft have been calculated (step 4) as described previously, these trajectories and density time-series can be used to create the guidance (step 5). This guidance is then tracked to create the relative maneuver (step 6). Three

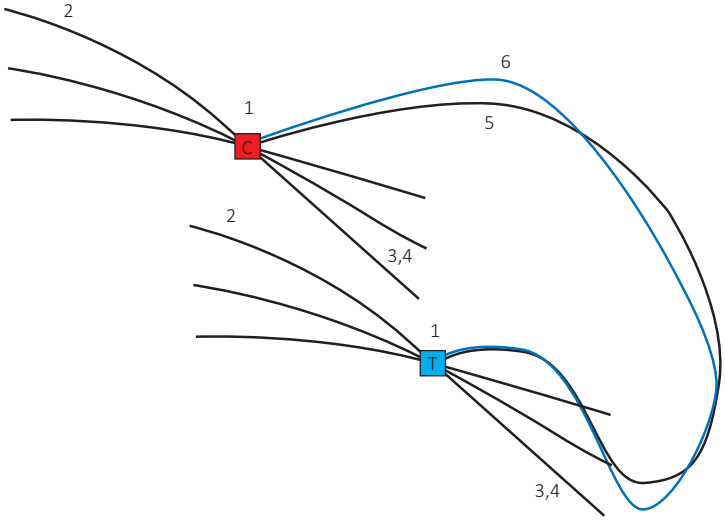

Figure 5. Concept of Calibrating and Forecasting Density, Followed by Guidance Creation and Tracking

additional guidance trajectories were created, each using the predicted density from only one of the three orbits along which the density was forecasted. The control law in Eqn. (9) is also used to create these guidances. These additional guidance allow the study of the benefit of utilizing the spatial resolution on the forecasted density provided by interpolating.

Tracking of the guidance relative trajectories is done using the same control law. The DTM-2013 density and the nonlinear dynamics in Eqn. (5) are used to propagate each spacecraft. At each timestep, the guidance position and velocity are used as the desired state to track the guidance.

NUMERICAL SIMULATIONS RESULTS

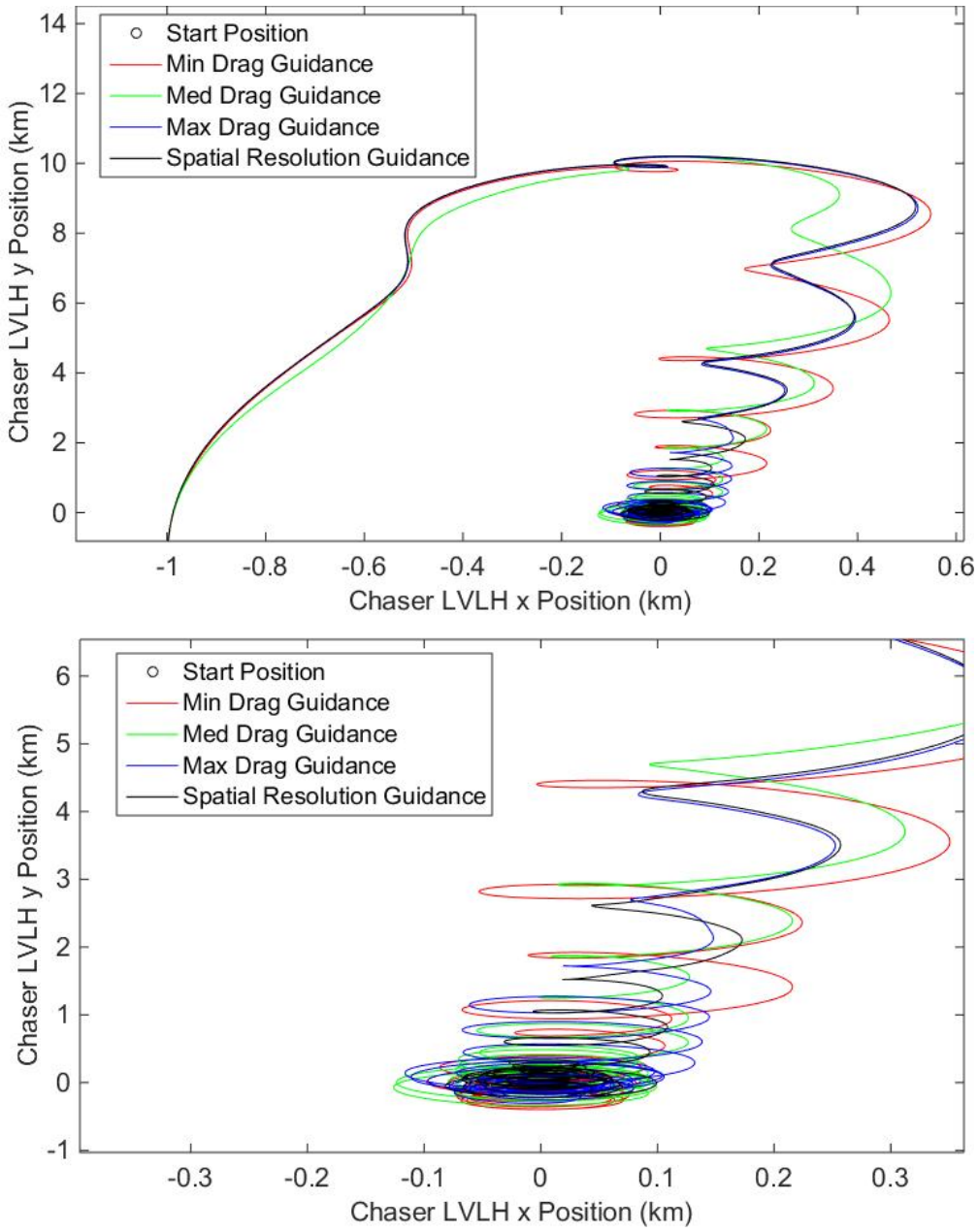

Figure 6. Rendezvous Trajectories in the *xy* Plane: (Top) Guidances Obtained With and Without the Interpolated Density and (Bottom) Detail View of Rendezvous Location, High K_p.

Figures 6 and 7 show all four guidance trajectories, while Figures 10 and 11 display the quadratic error function (Eqn. (8)), for the tracking of the four guidance trajectories. The functions seen in Figure 10 are smaller in the interpolated case, indicating that the controller can more easily force the nonlinear dynamics to follow the guidance trajectory generated with the interpolated density.

Guidance trajectories generated with a single trajectory case do not fully represent the complex behavior of the density. This highlights the advantage of using the spatial resolution. Figures 8 and 9 show the control trajectories resulting from tracking the best guidance in the high and low K_p cases.

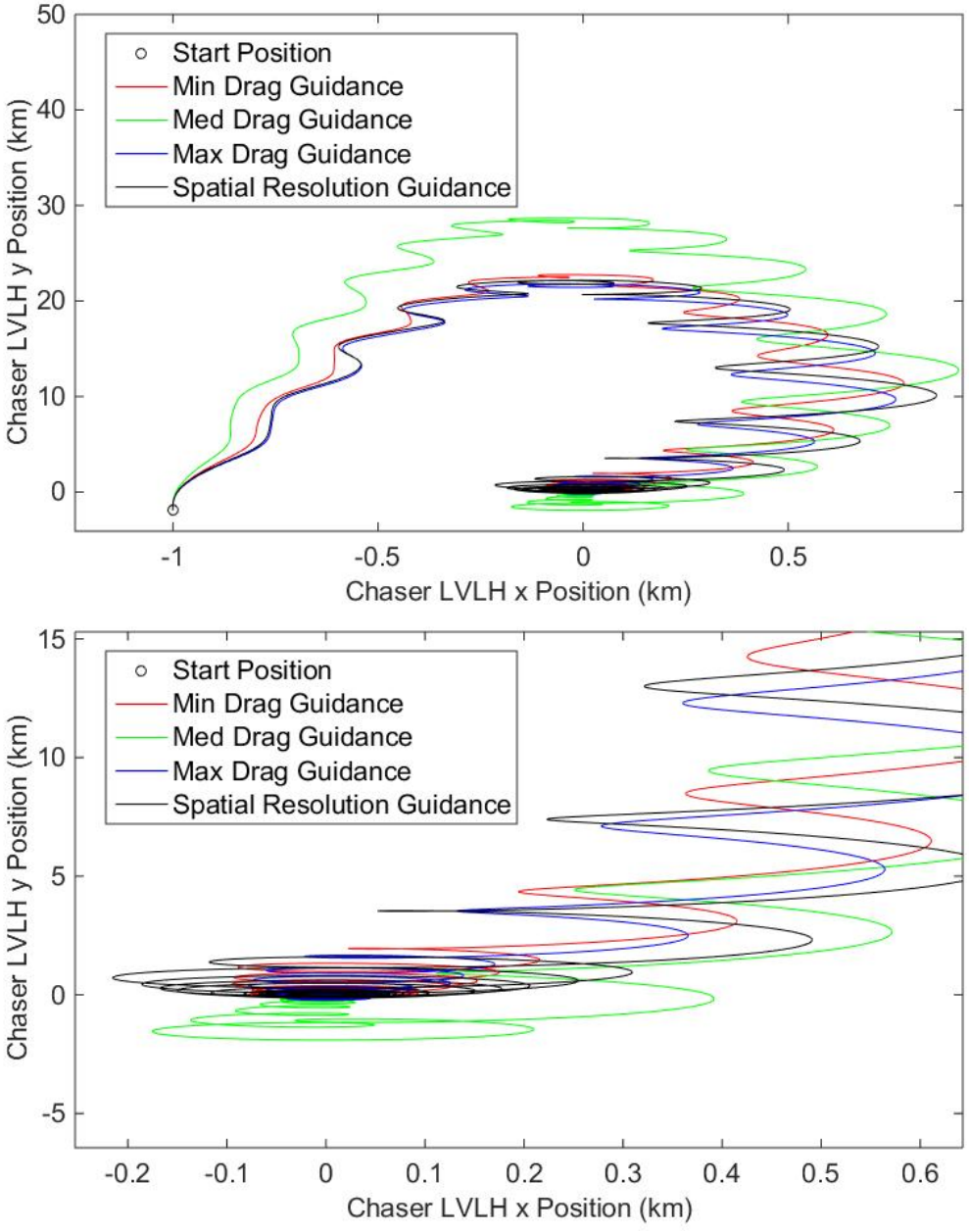

Figure 7. Rendezvous Trajectories in the *xy* Plane: (Top) Guidances Obtained With and Without the Interpolated Density and (Bottom) Detail View of Rendezvous Location, Low K_p.

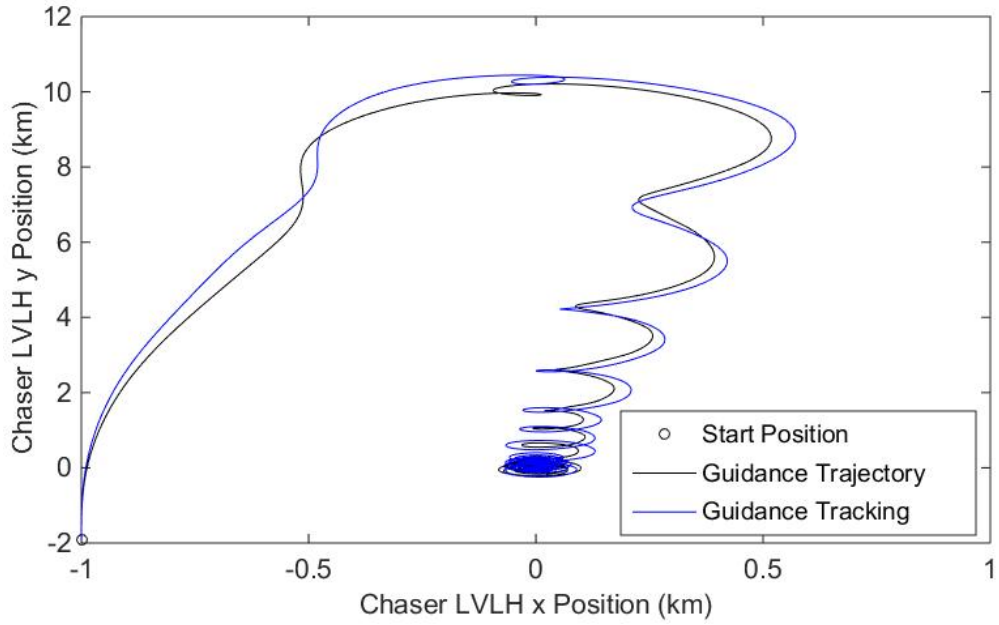

Figure 8. Tracking the Best Rendezvous Trajectory in the *xy* Plane, High K_p.

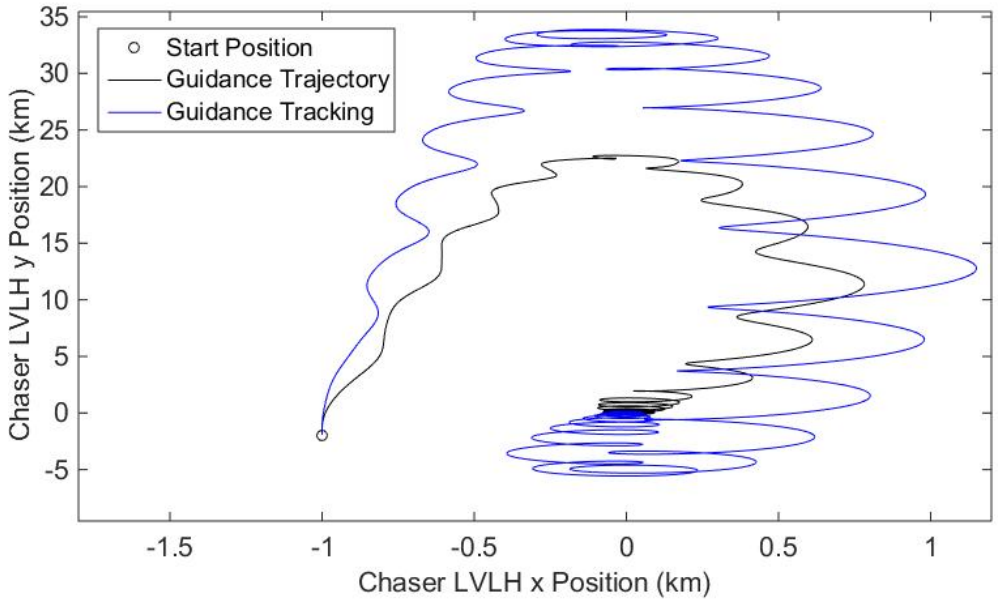

Figure 9. Tracking the Best Rendezvous Trajectory in the *xy* Plane, Low K_p.

Performance Assessment

The metrics used to evaluate the performance of the controllers (shown in Table 5) are the mean value of the quadratic error function and the number of changes in the control (control effort). Table 5 summarizes the actions of the controllers. The guidance generated with spatial resolution

in the high K_p case had the lowest mean value for the quadratic error function, implying that the guidance created with spatial resolution was easiest to track.

In the low K_p case, because of the low difference in semi-major axis of the orbits, there was significant overlap between cases in the forecasted density. The error of the networks could not be reduced to less than the difference in density between the drag cases; implementing the neural network predictors was unsuccessful in reducing the quadratic tracking error in the low K_p case due to the small difference between cases. Improving the network would not be useful for reducing the tracking error, since reducing the network error would begin to result in memorization of the training set.

Table 5. Control performance metrics for the rendezvous maneuver tracking the guidance obtained with the constant density and the predicted density from the neural network

Density Source	Metric	Guidance	Tracking
Interpolated, High K_p	Control changes	228	373
	Quadratic Error Function	-	$\mathbf{2.180 \cdot 10^3}$
Interpolated, Low K_p	Control changes	129	154
	Quadratic Error Function	-	$3.308 \cdot 10^6$
Min Drag, High K_p	Control changes	227	398
	Quadratic Error Function	-	$3.125 \cdot 10^3$
Min Drag, Low K_p	Control changes	116	133
	Quadratic Error Function	-	$3.283 \cdot 10^6$
Med Drag, High K_p	Control changes	225	392
	Quadratic Error Function	-	$3.823 \cdot 10^3$
Med Drag, Low K_p	Control changes	142	123
	Quadratic Error Function	-	$\mathbf{1.479 \cdot 10^6}$
Max Drag, High K_p	Control changes	226	325
	Quadratic Error Function	-	$3.342 \cdot 10^3$
Max Drag, Low K_p	Control changes	142	123
	Quadratic Error Function	-	$3.425 \cdot 10^6$

Figure 2 shows the K_p during the first 100 days of 2005. The increased atmospheric density results in increased separation between the forecasted trajectories due to more orbital decay in the higher drag cases, resulting in a potentially larger difference in the interpolated density. Increasing the separation through higher geomagnetic activity increases the spatial resolution accordingly, resulting in a larger benefit to adding spatial resolution.

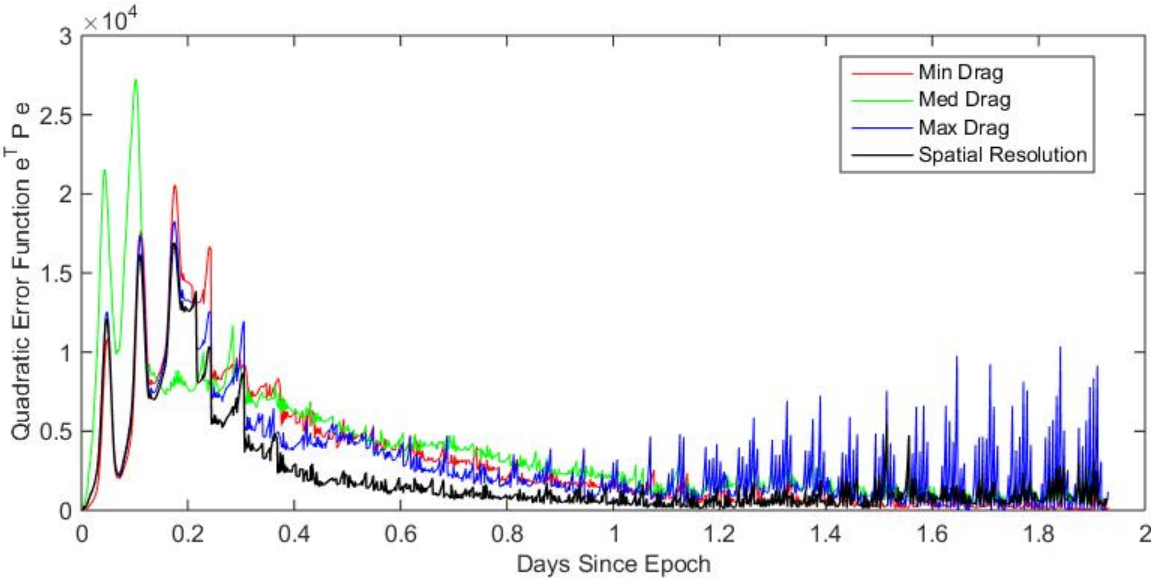

Figure 10. Quadratic Error Function $\vec{e^T}\underline{P}\vec{e}$ for All Cases, High K_p.

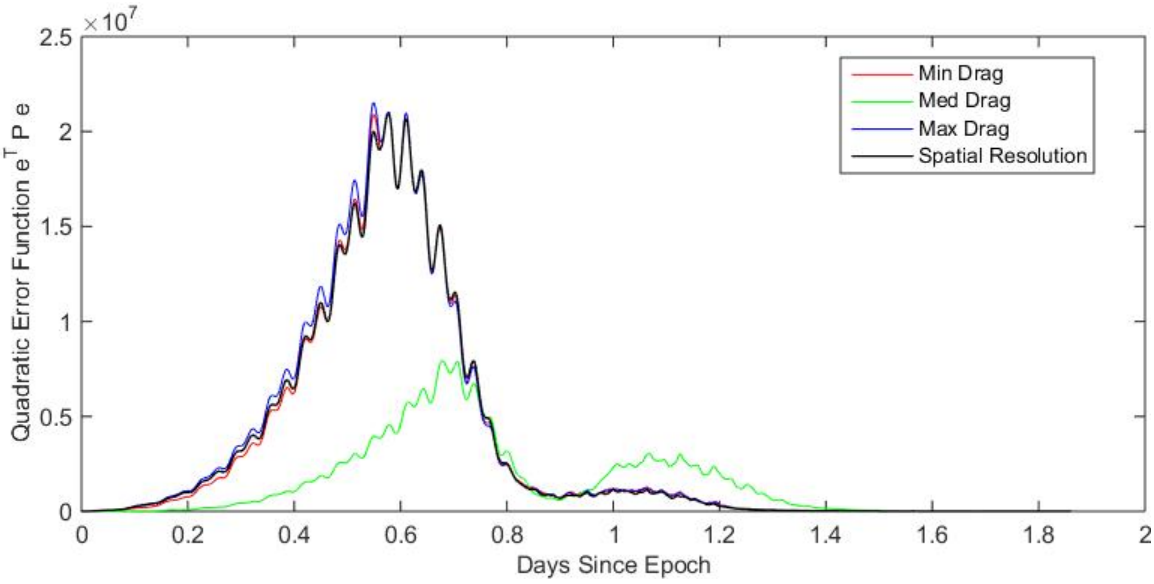

Figure 11. Quadratic Error Function $\vec{e^T}\underline{P}\vec{e}$ for All Cases, Low K_p.

CONCLUSION

Adding spatial resolution was shown to improve the tracking of differential-drag based guidances. The guidances created using a single forecasted trajectory to supply the density information were compared the guidance created using spatial resolution with all three forecasted trajectories. The quadratic error function was lowest when tracking the guidance created using spatial resolution in

the high K_p case, indicating that this guidance was easiest to track. Conversely, adding spatial resolution in the low K_p case prevented the creation of a consistent relative guidance and increased the tracking error when tracking the guidance created using spatial resolution.

The linear fit calibrator has been shown to successfully estimate DTM-2013 density from JB2008 and NRLMSISE-00 density at the same time and location. This allows it to be used as a proxy for DTM-2013, which represents the observed atmospheric density. Additionally, the predictors have successfully forecasted future density from past density. This forecasted density was then used to create three forecasted trajectories for the target and the chaser spacecraft, providing the spatial resolution mentioned above.

Improvements realized by adding spatial resolution have been shown to vary depending on the geomagnetic activity during maneuvers. Periods of high geomagnetic activity result in higher atmospheric density, producing larger separation between the forecasted trajectories. The larger separation then results in an increased benefit to adding spatial resolution.

Future work will address the generalization of this method to arbitrary maneuver epoch locations and times, as well as the incorporation of atmospheric activity indices such as K_p and $F10.7$ into the forecast of future density from past density.

ACKNOWLEDGMENT

The authors would like to acknowledge the United States Office of Naval Research (ONR) for sponsoring this investigation under the Young Investigator Program (Award no. N00014-13-1-0536).

NOTATION

A	Cross-wind area of drag surface
$\underline{A}$	State matrix from the Schweighart and Sedwick dynamics
$a_{D_{rel}}$	Magnitude of the relative aerodynamic drag acceleration experienced by spacecraft
$a_{J2_{rel}}$	Differential accelerations caused by the J_2 perturbations
a_{tar}	Mean semi-major axis of target spacecraft
$\underline{B}$	Gain matrix in controller
B	Ballistic coefficient
C_D	Drag Coefficient
$\vec{e}$	Tracking vector error
ECI	Earth-Centered Inertial
$f()$	Nonlinearities in the spacecraft dynamics
$F10.7$	10.7 solar radio flux, solar extreme ultraviolet radiation index
i_{tar}	Mean inclination of target spacecraft
J_2	Second zonal harmonic
K_p	Quantifies disturbances in the horizontal component of the Earth's magnetic field
$LVLH$	Local vertical local horizontal
m	Spacecraft mass
MSE	Mean Squared Error
n	Orbital frequency
$\underline{P}$	Constant gain matrix
r	Pearson correlation coefficient
$\vec{r}_n$	Relative position vector from the center of the ECI frame
r_n	Displacement from the center of the ECI frame
R_e	Mean equatorial radius of the Earth
$\hat{u}$	Control signal to spacecraft
UTC	Coordinated Universal Time
V	Lyapunov Function
$\dot{V}$	Time derivative of Lyapunov Function
$\vec{v}_T$	Velocity of the chaser spacecraft through a medium
$\vec{v}_T$	Velocity of the target spacecraft through a medium
$\vec{x}$	Position in the ECI frame
$\dot{\vec{x}}$	Velocity in the ECI frame
$\vec{x}_d$	Desired ECI Relative State
$\vec{x}_n$	Actual ECI Relative State
$\hat{x}, \hat{y}, \hat{z}$	LVLH frame unit vectors
X_n, Y_n, Z_n	Position in the ECI frame
$\dot{X}_n, \dot{Y}_n, \dot{Z}_n$	Velocity in the ECI frame
$\ddot{X}_n, \ddot{Y}_n, \ddot{Z}_n$	Acceleration in the ECI frame
μ	Universal gravitational parameter
ρ	Atmospheric density
ω	Orbital angular velocity

REFERENCES

[1] V. Kapila, A. G. Sparks, J. M. Buffington, and Q. Yan, "Spacecraft Formation Flying: Dynamics and Control," *AIAA Journal of Guidance, Control, and Dynamics*, Vol. 23, No. 3, 2000, pp. 561–564 http://dx.doi.org/10.2514/2.4567.

[2] C. Sabol, R. Burns, and C. A. McLaughlin, "Satellite Formation Flying Design and Evolution," *AIAA Journal of Spacecraft and Rockets*, Vol. 38, No. 2, 2001, pp. 270–278 http://dx.doi.org/10.2514/2.3681.

[3] D. Scharf, F. Hadaegh, and S. Ploen, "A Survey of Spacecraft Formation Flying Guidance and Control (Part 1): Guidance," *Proceedings of the 2003 American Control Conference*, Vol. 2, Jun 2003, pp. 1733–1739 http://dx.doi.org/10.1109/acc.2003.1239845.

[4] D. Scharf, F. Hadaegh, and S. Ploen, "A Survey of Spacecraft Formation Flying Guidance and Control (Part II): Control," *Proceedings of the 2004 American Control Conference*, Vol. 4, June 2004, pp. 2976–2985.

[5] H. Heidt, J. Puig-Suari, A. Moore, S. Nakasuka, and R. Twiggs, "CubeSat: A New Generation of Picosatellite for Education and Industry Low-Cost Space Experimentation," *Proceedings of the 14th Annual AIAA/USU Conference on Small Satellites*, September 2000, pp. 1–19.

[6] J. Puig-Suari, C. Turner, and R. Twiggs, "CubeSat: The Development and Launch Support Infrastructure for Eighteen Different Satellite Customers on One Launch," *Proceedings of the 15th Annual AIAA/USU Conference on Small Satellites, AIAA, Logan, UT*, August 2001, pp. 1–5.

[7] J. Puig-Suari, C. Turner, and W. Ahlgren, "Development of the Standard CubeSat Deployer and a CubeSat Class PicoSatellite," *Proceedings of the Aerospace Conference*, Vol. 1, March 2001, pp. 1347–1353 http://dx.doi.org/10.1109/aero.2001.931726.

[8] C. L. Leonard, W. M. Hollister, and E. V. Bergmann, "Orbital Formationkeeping with Differential Drag," *AIAA Journal of Guidance, Control and Dynamics*, Vol. 12, No. 1, 1989, pp. 108–113 http://dx.doi.org/10.2514/3.20374.

[9] R. Bevilacqua and M. Romano, "Rendezvous Maneuvers of Multiple Spacecraft by Differential Drag Under J_2 Perturbation," *AIAA Journal of Guidance, Control and Dynamics*, Vol. 31, No. 6, 2008, pp. 1595–1607 http://dx.doi.org/10.2514/1.36362.

[10] R. Bevilacqua, J. Hall, S., and M. Romano, "Multiple Spacecraft Assembly Maneuvers by Differential Drag and Low Thrust Engines," *Celestial Mechanics and Dynamical Astronomy*, Vol. 10, 2010, pp. 6988 http://dx.doi.org/10.1007/s10569--009--9240--3.

[11] S. A. Schweighart and R. J. Sedwick, "High-Fidelity Linearized J_2 Model for Satellite Formation Flight," *Journal of Guidance, Control, and Dynamics*, Vol. 25, No. 6, 2002, pp. 1073–1080 http://dx.doi.org/10.2514/2.4986.

[12] O. Ben-Yaacov and P. Gurfil, "Long-Term Cluster Flight of Multiple Satellites using Differential Drag," *Journal of Guidance, Control, and Dynamics*, Vol. 36, No. 6, 2013, pp. 1731–1740 http://dx.doi.org/10.2514/1.61496.

[13] D. Pérez and R. Bevilacqua, "Lyapunov-Based Adaptive Feedback for Spacecraft Planar Relative Maneuvering via Differential Drag," *AIAA Journal of Guidance, Control, and Dynamics*, Vol. 37, No. 5, 2014, pp. 1678–1684 http://dx.doi.org/10.2514/1.g000191.

[14] L. Dell'Elce and G. Kerschen, "Comparison between analytical and optimal control techniques in the differential drag based rendez-vous," *Proceedings of the 5th International Conference on Spacecraft Formation Flying Missions & Technologies*, 2013.

[15] L. Dell'Elce and G. Kerschen, "Optimal Propellantless Rendez-Vous Using Differential Drag," *Acta Astronautica*, Vol. 109, 2015, pp. 112 – 123 http://dx.doi.org/10.1016/j.actaastro.2015.01.011.

[16] T. D. Maclay and C. Tuttle, "Satellite Station-Keeping of the ORBCOMM Constellation Via Active Control of Atmospheric Drag: Operations, Constraints, and Performance," *Advances in the Astronautical Sciences*, Vol. 120, 2005, pp. 763–773.

[17] B. Kumar and A. Ng, *Japan Canada Joint Collaboration Satellite Formation Flying (JC2SatFF) Mission Design,*. 2013. Case Study.

[18] A. De Ruiter, J. Lee, and A. Ng, "A Fault-Tolerant Magnetic Spin Stabilizing Controller for the JC2SatFF Mission," *Acta Astronautica*, Vol. 68, August 2011, pp. 160–171 http://dx.doi.org/10.1016/j.actaastro.2010.07.012.

[19] B. Kumar, A. Ng, K. Yoshihara, and A. De Ruiter, "Differential Drag as a Means of Spacecraft Formation Control," *Proceedings of the 2007 IEEE Aerospace Conference, IEEE, Big Sky, MT*, March 2007, pp. 1–9 http://dx.doi.org/10.1109/aero.2007.352790.

[20] B. S. Kumar and A. Ng, "A Bang-Bang Control Approach to Maneuver Spacecraft in a Formation with Differential Drag," *Proceedings of the AIAA Guidance, Navigation and Control Conference and Exhibit, AIAA, Honolulu, HI*, August 2008, pp. 18–21 http://dx.doi.org/10.2514/6.2008.6469.

[21] M. W. Harris and B. Açıkmeşe, "Minimum Time Rendezvous of Multiple Spacecraft Using Differential Drag," *Proceedings of the AIAA Guidance, Navigation, and Control (GNC) Conference, AIAA, Boston, MA*, Vol. 10, August 2013, pp. 2372–2385 http://dx.doi.org/10.2514/1.61505.

[22] D. Pérez and R. Bevilacqua, "Feedback Control of Spacecraft Rendezvous Maneuvers Using Differential Drag," *Proceedings of the 4th International Conference on Spacecraft Formation Flying Missions & Technologies, Interscience, St-Hubert, Canada*, May 2011, pp. 1–10 http://dx.doi.org/10.2514/6.2011--6630.

[23] R. Bevilacqua, "Analytical Guidance Solutions for Spacecraft Re-Phasing Based on Input Shaping," *AIAA Journal of Guidance, Control, and Navigation*, Vol. 37, No. 3, 2014, pp. 1042–1047 http://dx.doi.org/10.2514/1.6000008.

[24] D. Pérez, *Adaptive Lyapunov Control and Artificial Neural Networks for Spacecraft Relative Maneuvering Using Atmospheric Differential Drag*. PhD thesis, Rensselaer Polytechnic Institute, 2013.

[25] D. Pérez, B. Wohlberg, T. Lovell, M. Shoemaker, and R. Bevilacqua, "Orbit-Centered Atmospheric Density Prediction Using Artificial Neural Networks," *Acta Astronautica*, Vol. 98, 2014, pp. 9–23 http://dx.doi.org/j.actaastro.2014.01.007.

[26] D. Pérez and R. Bevilacqua, "Neural Network Based Calibration of Atmospheric Density Models," *Acta Astronautica*, Vol. 110, 2015, pp. 58–76 http://dx.doi.org/10.1016/j.actaastro.2014.12.018.

[27] S. Bruinsma, "The DTM-2013 Thermosphere Model," *Journal of Space Weather and Space Climate*, 2015, p. A1 http://dx.doi.org/10.1051/swsc/2015001.

[28] J. M. Picone, A. E. Hedin, D. P. Drob, and A. C. Aikin, "NRLMSISE-00 Empirical Model of the Atmosphere: Statistical Comparisons and Scientific Issues," *Journal of Geophysical Research*, 2002 http://dx.doi.org/10.1029/2002ja009430.

[29] B. R. Bowman, W. K. Tobiska, F. A. Marcos, C. Y. Huang, C. S. Lin, and W. J. Burke, "A new empirical thermospheric density model JB2008 using new solar and geomagnetic indices," *Proceedings of the AIAA/AAS Astrodynamics Specialist Conference*, August 2008 http://dx.doi.org/10.2514/6.2008-6438.

[30] D. A. Vallado and D. Finkleman, "A Critical Assessment of Satellite Drag and Atmospheric Density Modeling," *Acta Astronautica*, Vol. 95, 2014, pp. 141–165 http://dx.doi.org/j.actaastro.2013.10.005.

[31] E. Doornbos, M. Förster, B. Fritsche, T. v. Helleputte, J. v. d. IJssel, G. Koppenwallner, H. Lühr, D. Rees, and P. Visser, "Air Density Models Derived from Multi-Satellite Drag Observations, Final Report," tech. rep., TU Delft, May 2009.

[32] Y. Deng and A. J. Ridley, "Possible Reasons for Underestimating Joule Heating in Global models: E Field Variability, Spatial Resolution, and Vertical Velocity," *Journal of Geophysical Research: Space Physics*, Vol. 112, 2007, pp. 1–20 http://dx.doi.org/10.1029/2006ja012006.

[33] N. B. Stastny, F. R. Chavez, C. Lin, A. T. Lovell, R. A. Bettinger, and J. Luck, "Localized Density/Drag Prediction for Improved Onboard Orbit Propagation," *Proceedings of the Advanced Maui Optical and Space Surveillance Technologies Conference, Curran Associates, Maui, HI*, September 2009, pp. 51–58.

[34] S. Bruinsma, J. M. Forbes, R. S. Nerem, and X. Zhang, "Thermosphere Density Response to the 2021 November 2003 Solar and Geomagnetic Storm from CHAMP and GRACE Accelerometer Data," *Journal of Geophysical Research: Space Physics*, Vol. 111, No. A6, 2006, pp. A06303, http://dx.doi.org/10.1029/2005JA011284.

[35] R. Walterscheid, "Solar Cycle Effects on the Upper Atmosphere-Implications for Satellite Drag," *AIAA Journal of Spacecraft and Rockets*, Vol. 26, No. 6, 1989, pp. 439–444 http://dx.doi.org/10.2514/3.26089.

[36] K. Alfriend, S. R. Vadali, P. Gurfil, J. How, and L. Breger, *Spacecraft Formation Flying: Dynamics, Control and Navigation*, Vol. 2. Butterworth-Heinemann, 2009.

[37] D. Pérez and R. Bevilacqua, "Lyapunov-Based Spacecraft Rendezvous Maneuvers Using Differential Drag," *Proceedings of the AIAA Guidance, Dynamics and Control Conference 2011, AIAA, Portland, OR*, August 2011, pp. 7231–7253 http://dx.doi.org/10.2514/6.2011--6630.